# Intrinsic Strength of Silicon Crystals in Pure- and Combined-Mode Fracture without Precrack

V. V. Kozhushko, A. M. Lomonosov, and P. Hess

*Institute of Physical Chemistry, University of Heidelberg, Im Neuenheimer Feld 253, D-69120 Heidelberg, Germany*

(Received 21 November 2006; published 11 May 2007)

Measurement of the critical fracture strength of single-crystal silicon was carried out by contact-free laser-based excitation and detection of nonlinear surface acoustic wave (SAW) pulses. The three crystallographic geometries Si(112)$\langle 11\bar{1}\rangle$, Si(112)$\langle \bar{1}\,\bar{1}\,1\rangle$, and Si(110)$\langle 1\bar{1}1\rangle$ were examined. A comparison of the optically detected SAW transients and numerically calculated stress-strain fields allowed an estimate of the intrinsic mechanical strength without using an artificial precrack. Depending on the geometry, the critical strength varied between 5 and 7 GPa.

DOI: 10.1103/PhysRevLett.98.195505 PACS numbers: 62.20.Mk, 46.50.+a, 62.30.+d

The strength of silicon is of increasing interest in technology and science. Silicon is the preferred material for sensors and devices such as microelectromechanical systems (MEMS), and as their size decreases the issue of scale in materials strength arises [1]. In several recent theoretical papers the ideal strength or elastic limit of silicon has been calculated [2–4]. The main drawback of these calculations is that only ideal systems were considered. Real silicon always contains impurities, dislocations, and other types of intrinsic defects, which decrease the strength; in contrast, the theoretical strength characterizes an ideal lattice or perfect crystal not available in practice.

A serious drawback of previous fracture experiments is the application of artificial precracks or notches to the specimen [5,6]. Most measurements have used quasistatic loads to reach the critical strain. This requires mechanical contact and a suitable geometry to realize a uniform stress field. With an artificial notch, propagation of an existing crack rather than nucleation is investigated [7]. While the directional anisotropy in the cleavage fracture of silicon has been studied theoretically [8,9], experimental results are lacking in general.

Previous fracture experiments indicated that crack nucleation started on the surface along the weakest Si{111} cleavage plane [10,11]. Crack nucleation occurs under a set of simultaneously acting tensile and shear stress components with their ratio determined by the inclination of the cleavage plane [10]. Mixed-mode processes complicate the understanding of crack nucleation. That is why geometries with the cleavage plane normal to the surface were chosen. In this Letter, dynamic fracture of silicon by nonlinear surface acoustic wave (SAW) pulses is studied for geometries where the maximal tensile stress is normal to the cleavage plane [10–12].

Nonlinear SAWs can produce shock fronts involving transient strains or stresses on the nanosecond time scale that exceed the critical fracture strength. Because of the extensive strain and the nonlinearity of silicon, the finite SAW pulses gain higher-frequency components during propagation by frequency up-conversion [13]. Note that it is much easier to reach strong nonlinearity with wideband pulses than with sinusoidal waves. The maximum tension or compression in the stress field, and thus crack nucleation, is always localized at the surface. As the SAW penetration depth is about one wavelength, the energy density at the surface grows with nonlinear SAW propagation. The optically detected SAW profiles and numerical solution of the nonlinear evolution equation were employed for stress-strain field calculations at the location of failure. The observed critical strength of silicon varies with the crystallographic plane and direction (''geometry'').

Excitation of SAW pulses with finite amplitudes was accomplished by the absorption-layer method [12–14]. The laser radiation of a 1.064 $\mu$m Nd:YAG laser with 30–160 mJ pulses with 8 ns duration was focused into a line of 8 mm length and $\sim$15 $\mu$m width to launch broadband SAW pulses with a plane wave front. This technique allowed the excitation of nanosecond SAW pulses with surface strains reaching $\sim$0.01 (''acoustic Mach number'') that evoke a nonlinear elastic response such as harmonic generation. The frequency spectrum of excited SAW pulses essentially depends on the width of the source line, thermophysical properties, and laser pulse duration.

The probe-beam deflection (PBD) technique was employed for SAW detection. A diode-pumped cw Nd:YAG laser radiating at 0.532 $\mu$m at $\sim$100 mW was used to monitor the transient slope of the surface. The laser beam was divided into two parts and each beam was sharply focused onto the surface with $\sim$4 $\mu$m spot size, one spot $\sim$1 mm from the source and the second at a distance of $\sim$17 mm. The frequency bandwidth of the setup was 5–500 MHz, limited by the finite size of the probe spot at the high-frequency side and by the electronics at its low-frequency side. The bandwidth limitation may result in a lower estimated stress since the high-frequency components are mainly responsible for the stress. The Si(112) and Si(110) planes of float-zone silicon with a typical miscut tolerance $<0.15°$ and surface resistance $>1000$ Ohm cm were used as delivered by CrysTec.

 

In silicon, the elastic properties depend on the crystal cut or free surface plane and the direction of SAW propagation along this plane. The linear elastic properties are described by three second-order elastic constants represented by the fourth-rank stiffness tensor $C_{ijkl}$, which has three independent components. Quadratic nonlinearity is characterized by the sixth-rank tensor $C_{ijklmn}$ containing six independent constants. The tensors of the second- and third-order elastic constants have to be transformed to the particular plane to provide the exact solutions for nonlinear evolution of SAWs [15]. The stress-strain relation can be applied in its linear form at any particular point to a very good approximation [16] $\sigma_{ij} = C_{ijkl}u_{kl}$, where the indices refer to the $x_1$, $x_2$, and $x_3$ axes, $u_i$ is the $i$th component of the particle displacement vector $\mathbf{u}(\mathbf{r}, t)$, $u_{ij} = \partial u_i/\partial x_j$, and $\sigma_{ij}$ is the stress tensor in symmetric form with the force acting in the direction of the $i$ axis on the unit area with orientation normal to the $j$ axis. Here $x_1$ points in the direction of wave propagation, the plane with $x_2 = 0$ defines the sagittal plane, and the $x_3$ axis is normal to the free crystal surface with the occupied region at $x_3 < 0$.

The signal $V(t)$ measured with the PBD setup is proportional to the surface slope $V = u_{31}/c$. To determine the coefficient of proportionality (calibration factor $c$) the set of nonlinear evolution equations was solved [17]

$$i\frac{\partial}{\partial\tau}B_n = nq_0\Bigg[\sum_{0<n'<n} F(n'/n)B_{n'}B_{n-n'} + 2\sum_{n'>n}(n/n')F^*(n/n')B_{n'}B^*_{n'-n}\Bigg], \quad (1)$$

where $B_n$ is the complex-valued amplitude of the $n$th harmonic of the signal $cV(t)$, $\tau$ is the propagation distance, $q_0$ is the fundamental wave number, and the kernel $F(x)$ is a dimensionless function that depends on the ratio of the second-order to third-order elastic constants of the selected geometry and describes the binary interaction of spectral components. It is defined over the segment $x \in [0, 1]$ and is symmetric about $x = 1/2$, so that $F(x) = F(1 - x)$.

In isotropic solids $F(x)$ is purely imaginary, whereas in crystals, with the exception of high-symmetry planes, it possesses a nonzero real part. In this case, the kernels $F_1$ and $F_2$ for counterpropagating waves are related by $F_1(x) = -F_2(x)^*$. The procedure of calculating $F(x)$ has been described previously [13,17]. This function describes the efficiency of frequency conversion, e.g., frequency upconversion, leading to an enrichment of high frequencies in the pulse spectrum. The calculations were carried out with the following normalization of the displacement vector component at the surface: $u_3(x_3 = 0) = 1$.

Numerical integration of Eqs. (1) over the distance between the two probe spots, with the waveform obtained at the first probe location as an initial condition, provides the prediction of the signal at any remote spot. By varying the calibration factor $c$ the predicted waveform was fitted to the measured one, thus obtaining the displacement gradient at the surface as $u_{31} = cV$. In certain geometries, for example Si(111)$\langle 11\bar{2}\rangle$ and Si(112)$\langle 11\bar{1}\rangle$, nonlinear evolution results in the formation of two narrow spikes or shock fronts, with the interval strongly dependent on the wave magnitude [18]. In the notation used hereafter the plane [e.g., (111)] indicates the free surface of the sample and the direction of SAW propagation is designated, for example, by $\langle 11\bar{2}\rangle$.

The distance between the two shocks in a SAW pulse was used as a fitting criterion, which makes the whole procedure more precise than applying an amplitude criterion. Note that $c$ depends only on the arrangement of the PBD setup and the reflectivity of the sample surface for the probe light. Therefore, once determined for a given material, it can be used for any orientation of the material because the signal is proportional to the surface gradient. We estimate the error of calibration to be below 10%.

It is always possible to evaluate the stress and strain fields at any point of the sample as the unique solution of the boundary problem for which the surface slope $u_{31}$ coincides with the measured one. The $\sigma_{11}$ stress component attains its maximum at the surface, whereas all other components have a smaller magnitude $\sigma_{21}$, $\sigma_{22} < \sigma_{11}$ or are equal to zero if the sagittal plane coincides with one of the high-symmetry planes [18].

The fracture induced by the stress field occurs along one of the planes of cleavage of the {111} type, which are normal to the sagittal plane. In order to calculate the crack driving conditions we transformed the stress tensor to the coordinate system associated with the crack (or the cleavage plane) with the $x_1^T$ axis normal to this plane and $x_2^T$ parallel to the free sample surface. In the rotated coordinate system the fracture modes I, II, and III are determined by the stresses $\sigma_{11}^T$, $\sigma_{31}^T$, and $\sigma_{21}^T$, respectively.

First, the results for the Si(112)[111] geometry are discussed. Here the kernel $F$ possesses a significant real part, which results in a very different type of nonlinear SAW evolution in opposite directions. The abrupt jump of the surface slope generated in the $\langle\bar{1}\,\bar{1}\,1\rangle$ direction is associated with a positive or tensile peak of $\sigma_{11}$. For Si(112)$\langle 11\bar{1}\rangle$ the measured $u_{31}$ transient has an $N$-type form that corresponds to two negative peaks or compression. As a result, the wave propagating in the $\langle\bar{1}\,\bar{1}\,1\rangle$ direction induced fracture at lower laser pulse energies than the reversal wave. The same behavior has previously been observed for the Si$(111)\langle\bar{1}\,\bar{1}\,2\rangle$ and Si(111)$\langle 11\bar{2}\rangle$ geometries, where the latter also exhibited an $N$-type profile of the transient [10].

For the Si(112)$\langle 11\bar{1}\rangle$ geometry the SAW profiles were recorded at probe spots 0.5 mm and 17.0 mm from the source. The calibration factor was obtained with the iterative procedure described above. Then the direction of propagation was reversed to Si(112)$\langle\bar{1}\,\bar{1}\,1\rangle$, and the SAW pulse was measured at the closest point to the source. As the calibration factor and SAW solution were known, the

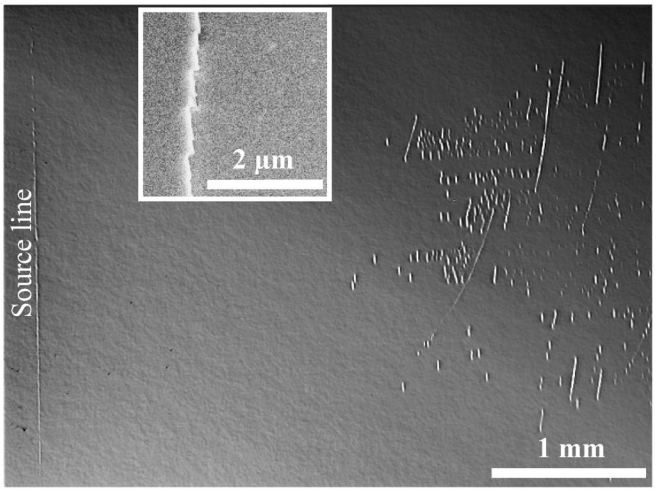


FIG. 1. Optical microscope image of the Si(112) surface after propagation of a nonlinear SAW pulse in the $\langle \bar{1}\,\bar{1}\,1\rangle$ direction. The inset shows part of a bent long crack, as obtained by secondary emission electron microscopy (steplike feature).

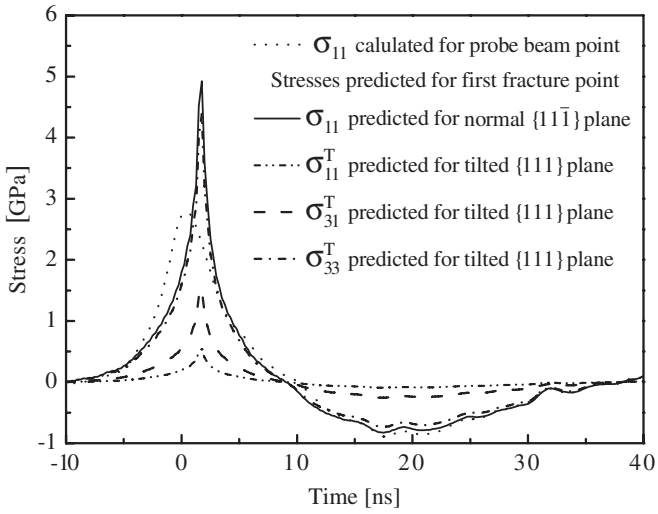


FIG. 2. Calculated stress components at the probe-beam spot for the Si(112)$\langle \bar{1}\,\bar{1}\,1\rangle$ geometry and stresses predicted at the first fracture point for the two cleavage planes.

stress-strain field could be calculated from the measured transient SAW profile and predicted for any other point. An optical image of a fractured Si(112) surface after SAW propagation in the $\langle \bar{1}\,\bar{1}\,1\rangle$ direction is presented in Fig. 1. The vertical line at the left side is the imprint of the exciting laser source. At a distance ~2 mm from the source the first crack is observed. Further propagation of the SAW pulse produced numerous cracks that extended into the $\langle 1\bar{1}0\rangle$ direction with a length of 50–100 $\mu$m. The analysis of the long bent crack features revealed that they consist of a set of small cracks along the $\langle 1\bar{1}0\rangle$ direction, similar to the steps of a stair (see inset of Fig. 1). In the Si(112)$\langle \bar{1}\,\bar{1}\,1\rangle$ geometry an extended crack field could be realized with a laser pulse energy of ~30 mJ.

The crack field results from repeated fracture processes occurring during pulse propagation, whenever the stress reaches the intrinsic strength of chemical bonding. The maximum of the strain energy is localized at the surface and decays into the depth exponentially. Note that fracture consumes mainly the high-frequency part of the pulse spectrum. After frequency up-conversion the critical stress is reached again during further propagation and so on. Note that silicon exhibits a phonon focusing effect for SAWs in the $\{mmn\}[nn\overline{2m}]$ geometries, where the directions of the group and phase velocities coincide.

There are two {111} cleavage planes in the sagittal section of the Si(112)$\langle \bar{1}\,\bar{1}\,1\rangle$ geometry. The first is perpendicular to the surface whereas the second is tilted at an angle of 19.5° to the surface. The normal plane of cleavage, $\{11\bar{1}\}$, is subjected to mode I load at the surface, since the only nonzero stress component is $\sigma_{11}$. The peak value of this stress was estimated as ~5 GPa. Figure 2 shows the time dependence of the corresponding measured and predicted stress components. For the other plane of cleavage, {111}, the load consists of contributions to mode I and mode II fracture. Their magnitudes are related to $\sigma_{11}$ by $\sigma_{11}^T(t) = 0.11\ \sigma_{11}(t)$ for mode I and $\sigma_{31}^T(t) = 0.31\ \sigma_{11}(t)$ for mode II with the peak values of 0.55 GPa and 1.5 GPa, respectively. Another nonzero component at the surface $\sigma_{33}^T(t) = 0.89\ \sigma_{11}(t)$ acts parallel to the fracture surface.

The Si(110)$\langle 1\bar{1}1\rangle$ geometry has a single cleavage plane perpendicular to the free surface. The nonlinear evolution generates a steep front of $u_{31}$, which corresponds to a positive tensile $\sigma_{11}$ peak. Besides this stress there are two other nonzero components at the surface, namely $\sigma_{21}$ and $\sigma_{22}$. The shear component $\sigma_{21}$ appears due to the fact that the sagittal plane is not parallel to the plane of mirror symmetry of the crystal, though its magnitude is relatively small with $\sigma_{11}/\sigma_{21} = 15$.

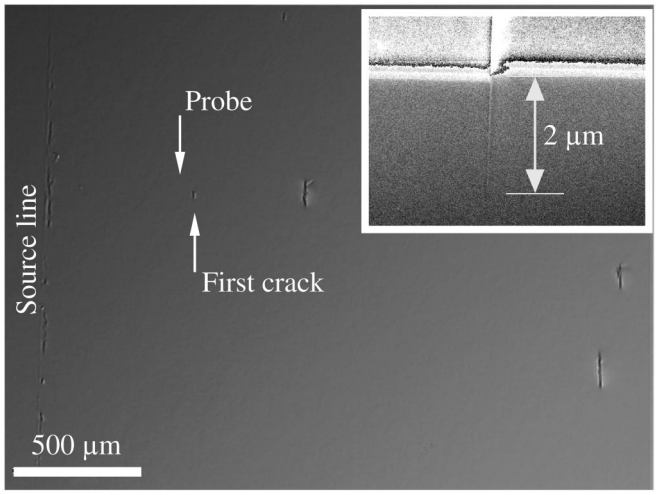


FIG. 3. Optical microscope image of the silicon surface after nonlinear SAW pulse propagation in the Si(110)$\langle 1\bar{1}1\rangle$ geometry. The inset shows a FIB image of in-depth crack propagation.

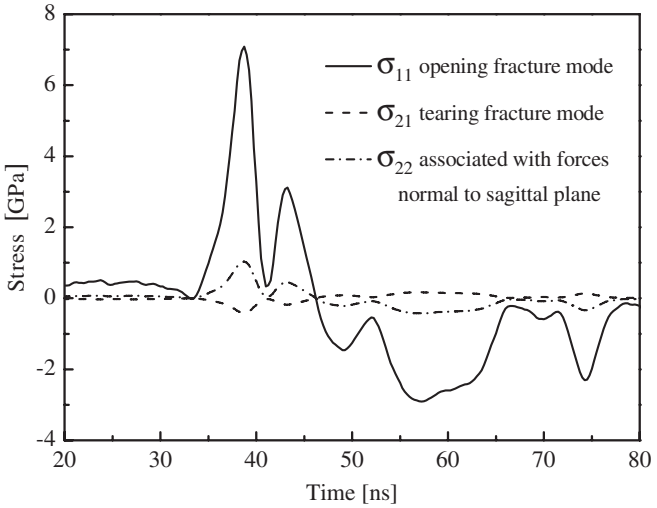


FIG. 4. Calculated stress components for the Si(110)⟨1$\bar{1}$1⟩ geometry.

In order to calculate the critical stress, the SAW pulse was measured close to the first crack, as indicated in Fig. 3. This figure presents an optical image of the fractured Si(110) surface. Since the probe beam was located near the first crack, the measured transient was employed to estimate the critical stress. The stress condition at the crack location consists of mode I load with a peak value of 7 GPa and mode III tearing load of 0.5 GPa. The temporal behavior of the relevant stress components is presented in Fig. 4. Besides the $\sigma_{11}$ and $\sigma_{21}$ components, a $\sigma_{22}$ stress component exists at the surface with a peak value of $\sim$1 GPa. This component stretches the material parallel to the surface crack. At a depth of several micrometers $\sigma_{33}$ and $\sigma_{31}$ come into play. Their local maxima are reached at about $\sim$10 $\mu$m depth.

In the Si(110)⟨1$\bar{1}$1⟩ geometry failure could be achieved only by increasing the laser pulse energy to $\sim$150 mJ, as compared to 30 mJ for weak fracture geometries. Only single cracks could be detected at distances $>$0.5 mm from the source with a length of 50–120 $\mu$m, as shown in Fig. 3. There is no crack field in this geometry. This can be explained by the lower nonlinearity and the absence of phonon focusing effects. Therefore, the diffraction losses are higher and the SAW pulse, after initial failure, could not easily reach the critical stress again. The FIB experiments clearly indicate that crack propagation was restricted to the Si{111} plane with penetration depths of 100 nm to 2.5 $\mu$m, as can be seen in the inset of Fig. 3. Obviously the stresses were sufficient for crack propagation into the depth, and one reason is the existence of the $\sigma_{21}$ stress component. In the case of low penetration it is possible that after instantaneous opening the crack closes again. The present experiments were not confined to two dimensions; however, penetration into the depth was substantially smaller than extension of the crack line along the surface.

In summary, notch-free dynamic fracture is introduced that allows the determination of the intrinsic strength of anisotropic materials for defined crystallographic geometries involving pure-mode and mixed-mode fracture. The stresses found for crack nucleation varied between 5 and 7 GPa, depending on geometry, and thus were lower than the calculated ideal tensile strength of 22 GPa [2]. Therefore, with nonlinear SAW pulses the intrinsic strength of real materials can be studied under transient dynamic load without any mechanical contact.

Financial support of this work by the Deutsche Forschungsgemeinschaft (DFG) is gratefully acknowledged.

[1] B. R. Lawn, J. Mater. Res. **19**, 22 (2004).
[2] D. Roundy and M. L. Cohen, Phys. Rev. B **64**, 212103 (2001).
[3] Y. Umeno and T. Kitamura, Mater. Sci. Eng. B **88**, 79 (2002).
[4] Y. Umeno, A. Kushima, T. Kitamura, P. Gumbsch, and J. Li, Phys. Rev. B **72**, 165431 (2005).
[5] T. Cramer, A. Wanner, and P. Gumbsch, Z. Metallkd. **90**, 675 (1999).
[6] J. A. Hauch, D. Holland, M. P. Marder, and H. L. Swinney, Phys. Rev. Lett. **82**, 3823 (1999).
[7] X. Li, T. Kasai, S. Nakao, T. Ando, M. Shikida, K. Sato, and H. Tanaka, Sens. Actuators A, Phys. **117**, 143 (2005).
[8] R. Pérez and P. Gumbsch, Phys. Rev. Lett. **84**, 5347 (2000).
[9] R. Péres and P. Gumbsch, Acta Mater. **48**, 4517 (2000).
[10] A. M. Lomonosov and P. Hess, Phys. Rev. Lett. **89**, 095501 (2002).
[11] G. Lehmann, A. M. Lomonosov, P. Hess, and P. Gumbsch, J. Appl. Phys. **94**, 2907 (2003).
[12] A. M. Lomonosov and P. Hess, J. Appl. Phys. **97**, 093528 (2005).
[13] A. M. Lomonosov, P. Hess, and A. P. Mayer, in *Modern Acoustical Techniques for the Measurement of Mechanical Properties*, edited by M. Levy, H. E. Bass, and R. Stern (Academic, New York, 2001), pp. 65–134.
[14] A. M. Lomonosov and P. Hess, Phys. Rev. Lett. **83**, 3876 (1999).
[15] M. F. Hamilton, Y. A. Il'inskii, and E. A. Zabolotskaya, J. Acoust. Soc. Am. **105**, 639 (1999).
[16] B. A. Auld, *Acoustic Fields and Waves in Solids* (Wiley, New York, 1973), Vol. I and II.
[17] C. Eckl, A. S. Kovalev, A. P. Mayer, A. M. Lomonosov, and P. Hess, Phys. Rev. E **70**, 046604 (2004).
[18] A. M. Lomonosov, P. Hess, R. E. Kumon, and M. F. Hamilton, Phys. Rev. B **69**, 035314 (2004).